Ad hoc tailored electrocatalytic MnO_2 nanorods for the oxygen reduction in aqueous and organic media

S. Orsini,[a] E. Pargoletti,[a,b,*] A. Vertova,[a,b,c] A. Minguzzi,[a,b,c] C. Locatelli,[a,b,c] S. Rondinini,[a,b,c] and G. Cappelletti[a,b]

[a] Università degli Studi di Milano, Dipartimento di Chimica, via Golgi 19, 20133, Milano, Italy

[b] Consorzio Interuniversitario Nazionale per la Scienza e Tecnologia dei Materiali (INSTM), via Giusti 9, 50121, Firenze, Italy

[c] ISTM-CNR, Istituto di Scienze e Tecnologie Molecolari, c/o Dipartimento di Chimica, Università degli Studi di Milano, via Golgi 19, 20133 Milano, Italy

E-mails: silvia.orsini2@studenti.unimi.it; alberto.vertova@unimi.it; alessandro.minguzzi@unimi.it; cristina.locatelli@unimi.it; sandra.rondinini@unimi.it; giuseppe.cappelletti@unimi.it.

Abstract

Metal-air batteries are one of the most promising electrochemical systems for energy storage and conversion. Herein we report promising results by exploiting manganese dioxide nanoparticles as ORR electrocatalysts. MnO_2 nanorods were prepared through a hydrothermal synthesis, *i.e.* by varying both the salt precursors (*i.e.* manganese sulphate or chloride) and the oxidizing agents (*i.e.* ammonium persulfate or potassium permanganate). All the nanopowders were finely characterized on structural, morphological and surface points of view. Then, their electrocatalytic power was tested either in aqueous 0.1 M potassium hydroxide or in Tetra Ethylene Glycol Dimethyl Ether (TEGDME)/$LiNO_3$ 0.5 M electrolytes, by using Gas Diffusion Electrodes (GDEs) and Glassy Carbon (GC) as cathodes, respectively. All the nanoparticles promoted the ORR by causing a shift of the onset potential up to 100 mV in both solvents. Nevertheless, this shift was different according to the solvent/electrolyte used: in the case of the ether-based solvent, different values are obtained by adopting the synthesized MnO_2 powders. Thus, we hypothesized that the structural/surface

* Corresponding author; Università degli Studi di Milano, Dipartimento di Chimica, via Golgi 19, 20133, Milano, Italy; e-mail: eleonora.pargoletti@unimi.it; Phone: +390250314210; Fax: +390250314228.

properties of MnO_2 samples are leveled in the aqueous medium (*i.e.* in a –OH rich solvent, the hydroxyls can interact with the homologs on the MnO_2 surface), contrary to what occurs in the organic solvent. Furthermore, a different behavior was observed also on the kinetic point of view thus leading to diverse interpretations of the oxygen reduction mechanism, especially in TEGDME.

Keywords

Manganese dioxide; electrocatalyst; aqueous medium; Tetra Ethylene Glycol Dimethyl Ether (TEGDME); Oxygen Reduction Reaction (ORR); metal-air devices.

1. Introduction

Nowadays, the contemporary society widely depends on the exploitation of reliable devices for the electrochemical energy storage/conversion. In particular, the consciousness of both the low-carbon economy and the environmental sustainability has greatly promoted the development of renewable chemical power sources, such as batteries and fuel cells [1]. Moreover, the progress in the long-range electrical vehicles field is strictly connected with the development of electrical supplies that can guarantee high energy density, low cost, increased safety and environmental compatibility [2]. For this purpose, one of the main fields being widely explored refers to metal-air batteries. Technologies like lithium-air or zinc-air batteries could deliver a much higher energy density with respect to the one obtained by the common lithium-ion devices [3]. For example, over the past decades, increased efforts have been made towards the development of aprotic Li-O_2 cells with the achievement of promising results [4], hence showing the great potential of these systems.

However, there are still some challenging aspects to deal with and, among them, there are two major problems to phase out: *i*) the slow kinetics of the Oxygen Reduction Reaction (ORR, which is the main cathodic reaction in metal-air batteries) that hinder the electrochemical performances of the final devices [5,6], and *ii*) the chemical stability of either the carbon cathodes or the solvent/electrolyte adopted [3,7]. For the former, a successful strategy to accelerate the ORR consists in using both metal and oxide-based electrocatalysts [8–12]. In this context, our group has largely employed cavity-microelectrodes [13,14] to rapidly characterize the electrocatalytic behavior of newly synthetized composite nanomaterials (for both oxygen reduction and evolution reactions), that can be used in metal-air batteries. As already demonstrated in

our previous work [15], the presence of α-MnO_2 nanoparticles can facilitate the cathodic reaction by shifting the onset potential of about 100 mV (value comparable to those obtained with the well-performing platinum-based electrocatalysts [16]). Nevertheless, these promising results were obtained in alkaline medium, which is not recommended in Li-air batteries, due to the different electrochemical reactions involving lithium and oxygen. Indeed, for this reason, the gravimetric and volumetric capacities of an aqueous Li-O_2 cell are much lower compared to those of an aprotic battery [17,18]. Hence, organic solvents should be utilized with a special consideration for their chemical stability during the charge/discharge cycles of the battery. Despite lots of attempts to find solvents that are stable towards the activated oxygen species (*i.e.* superoxides and peroxides that form during the oxygen reduction), none of them were found to be fully resistant [3]. Recent studies have reported that ethers are relatively stable solvents with low reactivity towards the superoxide ions [19], due to their high oxygen solubility and low dielectric constants. Moreover, as reported by Sharon *et al.* [3], the addition of $LiNO_3$ in polyether solutions can improve both the oxygen reduction and evolution reactions, since NO_3^- anions stabilize Li^+ cations that form during the discharge process.

Therefore, in this work we studied the electrocatalytic activity of novel manganese dioxide nanoparticles (synthesized starting from diverse salt precursors/oxidizing agents) both in alkaline and organic solvents. In particular, we adopted Tetra Ethylene Glycol Dimethyl Ether (TEGDME) as the organic medium [20], in the presence of lithium nitrate as the electrolyte, and we have either compared the shift of the onset oxygen reduction potential or studied the ORR on the kinetic/mechanistic points of view. As concerns the latter investigation, since literature about Tafel elaborations in the ether-based solvent is rather scarce [21], novel and promising results have been obtained.

2. Material and methods

All the chemicals were of reagent-grade purity and were used without further purification; doubly distilled water passed through a Milli-Q apparatus was utilized. All the reagents used were purchased from Sigma-Aldrich.

2.1 Synthesis of MnO_2 nanorods

In this work, a hydrothermal method previously optimized in our laboratory [15] was used, consisting in the reaction of stoichiometric manganese sulfate monohydrate ($MnSO_4.H_2O$) as the salt precursor, with ammonium persulfate ($(NH_4)_2S_2O_8$, MS_N compounds) or potassium permanganate ($KMnO_4$, MS_K samples) as the oxidizing agents. Moreover, by exploiting $KMnO_4$ oxidant, we also prepared MnO_2 nanoparticles starting from manganese chloride tetrahydrate ($MnCl_2.4H_2O$) precursor giving rise to MCl_K compounds. No further calcination steps were required, since all the washed [15] nanopowders have shown a high degree of crystallinity (see in the following).

2.2 Sample characterizations

X-Ray Powder Diffraction (XRPD) analyses were performed on a Philips PW 3710 Bragg-Brentano goniometer equipped with a scintillation counter, 1° divergence slit, 0.2 mm receiving slit and 0.04° soller slit systems. We employed graphite-monochromated Cu Kα radiation (Cu $K_{\alpha1}$ λ = 1.54056 Å, $K_{\alpha2}$ λ = 1.54433 Å) at 40 kV × 40 mA nominal X-rays power. Diffraction patterns were collected between 20° and 90° with a step size of 0.1° and a total counting time of about 1h. A microcrystalline Si-powdered sample was used as a reference to correct for instrumental line broadening effects.

Transmission Electron Microscope (TEM) analyses were performed on LIBRA 200 EFTEM (Zeiss) instrument operated at 200 kV accelerating voltage. The TEM grids were prepared dropping the dispersed suspension of nanoparticles in isopropanol onto a holey-carbon supported copper grid and drying it in air at room temperature overnight.

The BET surface area was determined by a multipoint BET method using the adsorption data in the relative pressure (p/p_0) range of 0.05-0.20 (Coulter SA3100 apparatus). Desorption isotherms were used to determine the total pore volume using the Barrett-Joyner-Halenda (BJH) method.

X-ray photoelectron spectra were obtained using a Mprobe apparatus (Surface Science Instruments). The source was the monochromatic Al Kα radiation (1486.6 eV); a spot size of 200 750 mm and a pass energy of 25 eV were used. The 1s level of hydrocarbon-contaminant carbon was taken as the internal reference at 284.6 eV. The accuracy of the reported binding energies (B. E.) can be estimated to be around 0.2 eV and the resolution is equal to 0.74 eV.

2.3 Fabrication of the Working Electrodes (WEs)

Different Working Electrodes (WEs) were used depending on the solvent/electrolyte used. In the case of water/0.1 M KOH electrolyte, Diffusion Electrodes (GDEs) fabricated following a general criterion already reported in our previous work [15] were utilized. Thus, a set of carbon slurries was prepared by mixing Carbon Vulcan XC- 72R (Cabot®), Shawinigan Acetylene Black AB50 Carbon (SAB, Chevron Philips) and each of the as-synthesized MnO_2 nanopowders, using Milli-Q water as solvent (solid materials/H_2O ratio equal to 0.025). The relative weight ratio among the components was: C Vulcan : MnO_2 : SAB : PTFE = 45 : 20 : 20 : 15, except for the reference GDEs which were prepared as follows: C Vulcan : SAB : PTFE = 65 : 20 : 15. After the complete wetting of the powders, a suspension of PTFE (10%wt in water, used as binder) was added. The slurry obtained was stirred for further 10 min and it was subsequently spread on a 4.5 × 4.5 cm^2 carbon cloth. The complete evaporation of water was achieved by leaving the GDEs in a stove for 20 min at 60°C. Finally, the electrodes were punched into 2.8 cm^2 disks with 2.2-3.4 mg cm^2 of active material. Instead, modified Glassy Carbon electrodes (GC by Amel, Italy; previously polished with diamond powder on a microcloth and rinsed with Milli-Q water) were adopted with Tetra Ethylene Glycol Dimethyl Ether (TEGDME)/0.5 M $LiNO_3$ electrolyte, since the present solvent permeates through the GDE pores. As concerns the latter, a set of carbon-based slurries has been prepared by mixing Carbon Vulcan XC-72R (Cabot®), each of the as-synthesized MnO_2 nanopowders and Nafion solution (5 %wt), using Milli-Q water as solvent (8 mL). The relative weight ratio among the components was: C Vulcan : MnO_2 : Nafion = 4.0 : 1.0 : 1.5, except for the reference GC electrode which was prepared as follows: C Vulcan : Nafion = 3.3 : 1.0. Then, the obtained slurries have been sonicated for 20 min and modified GC cathodes were prepared by drop casting (10 μL) of these suspensions. Finally, the electrodes have been dried under a fume hood overnight in order to evaporate the solvent. The differences in cathodes composition were due to the adopted medium. Indeed, the choice of an aqueous solvent along with the possibility to exploit GDE-type cathodes needs to use two types of carbons (*i.e.* Carbon Vulcan XC-72R and SAB) and PTFE as binder, in order to achieve better electrochemical performances. Actually, Maja *et al.* [22] stated that GDEs containing SAB and PTFE show higher hydrophobicity (a basic feature for metal-air batteries) and a more homogeneous structure with long-term durability.

The labeling of both the gas diffusion and glassy carbon electrodes followed that of the powders: for example, GDE(MS_N) or GC(MS_N) identify the electrodes prepared using the MS_N catalyst.

2.4 Electrochemical characterization

For the same reasons reported in the previous paragraph, we adopted different experimental apparatus according to the solvent/electrolyte used. In the presence of water/0.1 M KOH electrolyte, we utilized a home-made *H-cell* (Figure S1a) based on a Saturated Calomel Reference Electrode (SCE, R), inserted in a double-bridge filled with KNO_3 (Sigma-Aldrich ≥ 99%), and a Pt foil as the counter electrode (C). Instead, in the case of TEGDME/0.5 M $LiNO_3$ electrolyte, we exploited a three-electrodes conventional cell (Figure S1b) based on a silver wire quasi-Reference Electrode (Ag/Ag_2O, R) and a Pt foil as the counter electrode (C). Furthermore, unless otherwise stated, all the potentials will be rescaled to the Reversible Hydrogen Electrode (RHE) potential. High-purity oxygen was fed to the gas side of the GDEs or directly inside the three-electrodes conventional cell, both before (for 30 min) and during the electrochemical test (a bubbler was used to control the gas flux). The cell was studied by performing Staircase - Linear Sweep Voltammetries (*S*-LSVs) in the potential range between 0.0 and −1.0 V (*vs* SCE) or between 0.2 and –0.8 V (*vs* Ag/Ag_2O), and by evaluating the onset potential for the ORR (by extrapolating the first derivatives of the current density for aqueous tests and the intersection points for the organic ones, see Figure 4). *S*-LSVs were registered by applying a step potential of 10 mV for 10 s (in the case of the aqueous solvent) or for 3 s (in the case of the organic medium, TEGDME) to obtain a scan rate of 1 mV s^{-1} or about 3 mV s^{-1} respectively, recording the current at the end of each potential step. Moreover, in order to have a blank reference the same electrochemical tests were conducted in an inert atmosphere.

An Autolab PGSTAT101 potentiostat/galvanostat was employed to perform *S*-LSV tests and Nova 1.11 software was used for data acquisition.

3. Results and Discussion

3.1 Physico-chemical characterizations of MnO_2 nanopowders

The tailoring of the adopted synthetic route has deeply influenced the physico-chemical features of the final MnO_2 nanopowders, such as the structural composition. Several distinct polymorphs of manganese

dioxide (stoichiometric and not) have been widely classified and reported in the literature [23–26]. Therefore, XRPD technique was employed to investigate the structure of the as-synthesized powders. All the X-ray spectra have quite well-defined peaks without broad shoulders (Fig. 1), thus indicating a significant degree of crystallinity notwithstanding the rather low temperatures involved in the process. By studying the X-ray diffraction data, all the prepared nanopowders are mainly composed by two polymorphs (*i.e.* α-MnO_2 and β-MnO_2 ramsdellite, see Fig. 1). In particular, both MS_N and MCl_K spectra show a quite sharp peak at low angles (2θ at around 22°) ascribable to the 100% intensity reflection plane of β-MnO_2 ramsdellite polymorph; whereas MS_K X-ray line is not characterized by any traces of this phase. Therefore, K^+ ions (deriving from potassium permanganate, MS_K), compared to NH_4^+ (from ammonium persulfate, MS_N), could preferentially adsorb or enter into MnO_2 crystal lattice favoring the growth of the α-polymorph [15]. Nevertheless, in the present study, we also wanted to focus on the role played by the Mn^{2+} precursors. By comparing MS_K and MCl_K samples, which have the same oxidizing agent but different manganese precursor, an appreciable amount of the ramsdellite polymorph in the latter powder can be observed. Indeed, according to Huang *et al.* [27], α- and β-MnO_2 could be *ad hoc* synthesized via a hydrothermal reaction between $MnCl_2$ and $KMnO_4$, by varying the amount of K^+ or H^+ cations. Their experimental results showed the higher the potassium cations concentration with respect to the H^+ one, the higher the formation of the α-phase and vice versa.

On the morphological point of view, TEM images have revealed the presence of nanorods with lengths up to several hundred of nanometers and diameters of 20-30 nm, for all the synthesized MnO_2 powders (Fig. 2).

As concerns the nanoparticles surface features (see Figure 3), MS_K sample shows both the highest surface area (116 $m^2\ g^{-1}$) and total pore volume (0.895 $cm^3\ g^{-1}$). Indeed, by comparing MS_K with MCl_K (S_{BET} = 69 $m^2\ g^{-1}$ and $V_{\text{tot. pores}}$ = 0.576 $cm^3\ g^{-1}$) nanopowders we have noticed that, by keeping constant the oxidizing agent (*i.e.* $KMnO_4$), the pivotal role is played by the anions of the Mn^{2+} precursors. Actually, SO_4^{2-} groups (from manganese sulphate) may interact with the hydroxyl groups on MnO_2 surface preventing further aggregation of the manganese dioxide particles, as also reported by Wang *et al.* in the case of manganese acetate used as Mn^{2+} precursor [28]. On the contrary, MS_N sample has both the lowest surface area and total pore volume (Figure 3). In this case, since we used the same salt precursor (*i.e.* $MnSO_4$) but a

different oxidant, we hypothesized that the presence of bigger cations (NH_4^+ *vs* K^+), characterized by slightly different hydrated radii [15,29], could lead to a more expanded lattice [29]. Moreover, notwithstanding Figure 3 shows that the majority of pores are in the range between 20 and 60 nm, MS_K sample has a higher number of mesopores (with diameter between 6 and 20 nm), which are typical of this kind of nanomaterials [7,30].

3.2 Electrocatalytic evaluation of MnO_2 nanorods in the WEs

To evaluate the electrocatalytic properties of the synthesized MnO_2 nanoparticles, Gas Diffusion Electrodes (GDEs) or modified Glassy Carbons (GCs) were prepared and used as cathodes, depending on the adopted solvent. Thus, their electroactivity was determined by means of *S*-LSVs, both in the aqueous (KOH 0.1 M) and organic (TEGDME/$LiNO_3$ 0.5 M) media. According to the literature [10,15,31–33], a shift of the ORR onset potential towards less cathodic values was expected in order to have a performing catalyst.

Hence, starting from *S*-LSV scans in the aqueous solvent, the potential shift obtained with MnO_2-modified GDEs is about 100 mV less cathodic than the one got with bare cathode (see Table 1 and Fig. 4a). This is a promising result if compared to the other electrocatalysts reported in the literature [15,16,34]. Indeed, no significant differences for the ORR onset potentials in the aqueous electrolyte could be noticed by varying both the salt precursors and the oxidizing agents. Furthermore, GDE(MS_K) showed lower diffusive limitations since the corresponding current density values, at a given potential (in particular between 0.0 and 0.5 V *vs* RHE), are much higher than those obtained with the other MnO_2 nanoparticles (Fig. 4a). We have already reported [15] that this behavior is strictly connected with the oxygen permeability through the cathode pores, which in turn is related to the MnO_2 pores volume (Figure 3), since the carbonaceous matrix remained unchanged and only manganese dioxide nanoparticles were varied. Thus, MCl_K sample showed an intermediate electrocatalytic response, underlining once more the pivotal role played by the surface parameters (*i.e.* surface areas and total pore volumes, Fig. 3) that have been tailored by using different salt precursors or oxidizing agents.

Once deeply investigated the MnO_2 nanopowders behavior in the aqueous medium, our attention was focused on their electrocatalytic response in TEGDME. In this case, differently from the water solvent, the three synthesized manganese dioxide nanoparticles led to a diverse shift of the ORR onset potential (Figure

4b and Table 1). In particular, the most performing sample in terms of both the greatest onset shift and the lowest diffusive limitations, seems to be MS_K, followed digressively by MCl_K and MS_N powders. Therefore, we hypothesized that the synthesized MnO_2 nanoparticles have a different affinity for the adopted organic solvent. Specifically, from O 1s XPS results (Table 2 and Figure S2) we observed the presence for all the nanopowders of peaks at around 531 and 532 eV [29,30], which can be assigned to hydroxyl groups and chemisorbed water, respectively. Thus, we assumed that the structural/surface properties of MnO_2 samples are leveled in the aqueous medium (due to the presence of the hydroxyls that can interact with the homologs on the MnO_2 surface); whereas in a –OH poor solvent (such as TEGDME), these physico-chemical surface characteristics can play a pivotal role in influencing the nanoparticles electrocatalytic behavior, thus favoring the possible adsorption of O_2 molecules on the manganese active sites.

Furthermore, kinetic parameters have been determined through Tafel elaborations of the registered *S*-LSV scans (Figure 5). Concerning the tests in aqueous medium, a further corroboration of our previous work [15] has been obtained. Indeed, Tafel slopes (-*b* values, Table 1, 4th column) determined in the range 0.5 – 1.0 V (*vs* RHE, Figure 5a) allowed to evaluate the different electrocatalytic behavior of the MnO_2-modified GDEs. Actually, the addition of manganese dioxide caused an increase of *b* values from ~60 mV dec^{-1} to 90 – 100 mV dec^{-1} for GDE(MS_K) and GDE(MS_N) samples, whereas the increment was a little bit higher (up to 160 mV dec^{-1}) for GDE(MCl_K). This fact has been widely reported in literature for MnO_2-modified GDEs used in the same range of overpotentials under traditional conditions (*i.e.* at relatively high overpotentials, both in acidic and basic aqueous media) [31,35–37].

On the contrary, Tafel slopes values in TEGDME/$LiNO_3$ medium showed a peculiar trend (Figure 5b and Table 1, 4th column). At low current densities, the presence of all the three MnO_2 nanopowders provoked a decrease of the *b* values down to ~30 mV dec^{-1} (*i.e.* RT/2F, half of the Nernstian slope). On the mechanistic point of view, according to V. Jovancicevic and O. M. Bockris work [38], we hypothesized that the oxygen reduction in the adopted organic solvent occurs through the formation of adsorbed lithium superoxide (LiO_2) and peroxide (Li_2O_2) species on the cathode surface active sites. In particular, since GC without MnO_2 showed a *b* value of ~40 mV dec^{-1}, we assumed the main role played by manganese dioxide electrocatalytic powders in the Li_2O_2 formation/desorption. Indeed, the possible reactions occurring in the reduction process could be:

(1) $O_2 + e^- + M \Leftrightarrow O_2^-–M$ (M = active sites)

(2) $O_2^-–M + Li^+ + e^- \Leftrightarrow LiO_2^-–M$

(3) $LiO_2^-–M + Li^+ \Leftrightarrow Li_2O_2–M$

By hypothesizing both that *i*) the 3rd step (*i.e.* formation of lithium peroxide) is the rate determining step (*rds*, whereas steps 1 and 2 are in pre-equilibrium) and *ii*) the adsorption of oxygen superoxide/peroxide species can be approximated to the Langmuir type θ (coverage degree) $\rightarrow$ 0 [38], it is possible to infer that:

$$i_{\text{step 3}} = F \cdot k_3 \cdot \theta_{LiO_2^-} \cdot c_{Li^+} \qquad \text{(Eq. 1)}$$

where F is the Faraday constant, k_3 is the rate constant of reaction 3, $\theta_{LiO_2^-}$ is the fraction of surface covered by LiO_2^- species and c_{Li+} is lithium ion concentration. Since reactions 1 and 2 are assumed to be in equilibrium, it is possible to calculate $\theta_{LiO_2^-}$ as follows:

$$\theta_{LiO_2^-} = \frac{k_1}{k_{-1}} \cdot \frac{k_2}{k_{-2}} \cdot c_{Li^+} \cdot P_{O_2} \cdot \exp\left(-\frac{2F\eta}{RT}\right) \qquad \text{(Eq. 2)}$$

where k_1, k_{-1}, k_2, k_{-2} are the rate constants for reaction 1 and 2, respectively and P_{O2} is the oxygen partial pressure. Hence, by combining Equation 2 into Equation 1, we obtain:

$$\frac{\partial \eta}{\partial \log(i)} = 2.303 \frac{RT}{2F} \qquad \text{(Eq. 3)}$$

that is the expression of the Tafel slope (where i is the current, η the overpotential and T the temperature that we assumed equal to 298 K). On the contrary, when the reaction 2 (which is an electron transfer reaction) is the *rds* and symmetry factor is equal to 0.5 [39], the expression of the Tafel slope becomes:

$$\frac{\partial \eta}{\partial log(i)} = 2.303 \frac{RT}{(1+0.5)F} \qquad \text{(Eq. 4)}$$

therefore obtaining a value of 40 mV dec^{-1}. Indeed, for GC without MnO_2 nanoparticles a similar value was obtained (Figure 5b and Table 2, 4th column), thus indicating that in the absence of the electrocatalytic nanopowders the *rds* is the electron transfer reaction between the electrode and the chemical species. On the contrary, the presence of MnO_2 strongly favored the electron transfer reactions (steps 1 and 2), and hindered the reaction 3 (*i.e.* the chemical formation of lithium peroxide), which we assumed to be the *rds* of the entire process.

4. Conclusions

In the present work, manganese dioxide nanoparticles with tailored physico-chemical features have been synthesized by varying both the salt precursors and the oxidizing agents. *Ad hoc* MnO_2 have been subsequently applied as cathode electrocatalysts either in water/0.1 M KOH or TEGDME/0.5 M $LiNO_3$ electrolytes, thus obtaining very promising results in the oxygen reduction reaction potentials shift towards less cathodic values.

Three different MnO_2 nanopowders were successfully synthesized using ammonium persulfate/potassium permanganate as the oxidizing agents, whereas manganese sulphate and chloride were adopted as the salt precursors. As stated in our previous study [15], oxidants cations can play a pivotal role in modifying the structural, morphological and surface properties of the final nanopowders. Nevertheless, herein we further investigated the tailoring of these physico-chemical features by changing also the starting salt. Specifically, all the synthesized nanorods had α-MnO_2 as the main polymorph (confirmed by XRPD), with a small percentage of the ramsdellite phase for MS_N and MCl_K samples. By contrast, a great difference has been found investigating their surface properties. In particular, the combination of potassium permanganate and manganese sulphate (MS_K) has led both to the highest surface area (116 $m^2\ g^{-1}$) and pore volume (0.895 $cm^3\ g^{-1}$): two parameters that turned out to be fundamental for their electrocatalytic performances.

Then, both MnO_2-modified GDEs and GC were prepared and tested in aqueous and organic media, respectively. By means of *S*-LSV scans, we have observed that: *i*) the presence of manganese dioxide nanoparticles led to a shift of the onset oxygen reduction potential, in both solvents; *ii*) this shift is equal to 100 mV for all the nanopowders in aqueous KOH, whereas it differs in TEGDME (the greatest one is achieved with MS_K sample, *i.e.* 107 mV) therefore highlighting the O_2/solvent/MnO_2 interactions; *iii*) MS_K seems to be also characterized by less diffusive limitations (probably due to the much higher O_2 permeability, which is strictly related to MS_K greatest pore volume).

Furthermore, on the kinetic/mechanistic points of view, novel and interesting observations have been made for MnO_2 behaviour in TEGDME/$LiNO_3$ since a Tafel slope of about 30 mV dec^{-1} (half of the Nernstian slope) has been determined for all the three samples, under the above-mentioned approximations. On the contrary, if the electron transfer described by reaction 2 is the *rds*, the Tafel slope increases up to 40 mV dec^{-1}, which is the value obtained in the absence of MnO_2. Hence, at low current densities in the

presence of electrocatalytic powders, the electron transfer processes are favored thus hindering lithium peroxide formation.

Acknowledgements

Dr. Marcello Marelli from CNR-ISTM/ISTeM is gratefully acknowledged for TEM measurements.

Conflict of Interest: The authors declare that they have no conflict of interest.

References

[1] F. Cheng, J. Chen, Metal–air batteries: from oxygen reduction electrochemistry to cathode catalysts, Chem. Soc. Rev. 41 (2012) 2172. doi:10.1039/c1cs15228a.

[2] N. Akhtar, W. Akhtar, Prospects, challenges, and latest developments in lithium–air batteries, Int. J. Energy Res. (2007). doi:10.1002/er.3230.

[3] D. Sharon, D. Hirsberg, M. Afri, F. Chesneau, R. Lavi, A. a. Frimer, et al., Catalytic Behavior of Lithium Nitrate in Li-O_2 Cells, ACS Appl. Mater. Interfaces. 7 (2015) 16590–16600. doi:10.1021/acsami.5b04145.

[4] R. Younesi, G.M. Veith, P. Johansson, K. Edstrom, T. Vegge, Lithium salts for advanced lithium batteries: Li-metal, Li-O_2, and Li-S, Energy Environ. Sci. 8 (2015) 1905–1922. doi:10.1039/C5EE01215E.

[5] M.S. Hegde, G. Madras, K.C. Patil, Noble Metal Ionic Catalysts, Acc. Chem. Res. 42 (2009) 704–712. doi:10.1021/ar800209s.

[6] N.N. Opembe, C.K. King'ondu, A.E. Espinal, C.-H. Chen, E.K. Nyutu, V.M. Crisostomo, et al., Microwave-Assisted Synthesis of Manganese Oxide Octahedral Molecular Sieve (OMS-2) Nanomaterials under Continuous Flow Conditions, J. Phys. Chem. C. 114 (2010) 14417–14426. doi:10.1021/jp104699p.

[7] A. Minguzzi, G. Longoni, G. Cappelletti, E. Pargoletti, C. Di Bari, C. Locatelli, et al., The Influence of Carbonaceous Matrices and Electrocatalytic MnO_2 Nanopowders on Lithium-Air Battery Performances, Nanomaterials. 6 (2016) 10. doi:10.3390/nano6010010.

[8] Z. Zhang, M. Li, Z. Wu, W. Li, Ultra-thin PtFe-nanowires as durable electrocatalysts for fuel cells, Nanotechnology. 22 (2011) 15602. doi:10.1088/0957-4484/22/1/015602.

[9] J. Cao, Q. Mao, L. Shi, Y. Qian, Fabrication of γ-MnO_2/α-MnO_2 hollow core/shell structures and their application to water treatment, J. Mater. Chem. 21 (2011) 16210. doi:10.1039/c1jm10862j.

[10] K. Guo, Y. Li, J. Yang, Z. Zou, X. Xue, X. Li, et al., Nanosized Mn–Ru binary oxides as effective bifunctional cathode electrocatalysts for rechargeable Li–O_2 batteries, J. Mater. Chem. A. 2 (2014) 1509–1514. doi:10.1039/C3TA13176A.

[11] C. Locatelli, A. Minguzzi, A. Vertova, S. Rondinini, IrO_2–SnO_2 mixtures as electrocatalysts for the

oxygen reduction reaction in alkaline media, J. Appl. Electrochem. 43 (2013) 171–179. doi:10.1007/s10800-012-0520-3.

[12] D.S. Kim, Y.J. Park, Effect of multi-catalysts on rechargeable Li–air batteries, J. Alloys Compd. 591 (2014) 164–169. doi:10.1016/j.jallcom.2013.12.208.

[13] A. Minguzzi, C. Locatelli, G. Cappelletti, C.L. Bianchi, A. Vertova, S. Ardizzone, et al., Designing materials by means of the cavity-microelectrode: the introduction of the quantitative rapid screening toward a highly efficient catalyst for water oxidation, J. Mater. Chem. 22 (2012) 8896. doi:10.1039/c2jm15750k.

[14] A. Minguzzi, C. Locatelli, G. Cappelletti, M. Scavini, A. Vertova, P. Ghigna, et al., IrO_2-Based Disperse-Phase Electrocatalysts: A Complementary Study by Means of the Cavity-Microelectrode and Ex-Situ X-ray Absorption Spectroscopy, J. Phys. Chem. A. 116 (2012) 6497–6504. doi:10.1021/jp212310v.

[15] E. Pargoletti, G. Cappelletti, A. Minguzzi, S. Rondinini, M. Leoni, M. Marelli, et al., High-performance of bare and Ti-doped α-MnO_2 nanoparticles in catalyzing the Oxygen Reduction Reaction, J. Power Sources. 325 (2016) 116–128. doi:10.1016/j.jpowsour.2016.06.020.

[16] J.J. Salvador-Pascual, V. Collins-Martínez, A. López-Ortíz, O. Solorza-Feria, Low Pt content on the $Pd_{45}Pt_5Sn_{50}$ cathode catalyst for PEM fuel cells, J. Power Sources. 195 (2010) 3374–3379. doi:10.1016/j.jpowsour.2009.12.045.

[17] J. Lu, L. Li, J.-B. Park, Y.-K. Sun, F. Wu, K. Amine, Aprotic and Aqueous Li–O_2 Batteries, Chem. Rev. 114 (2014) 5611–5640. doi:10.1021/cr400573b.

[18] P. Albertus, J.F. Christensen, T. Lohmann, Aqueous Li/O_2 Battery with Water Storage, 20150357693, 2015.

[19] I. Gunasekara, S. Mukerjee, E.J. Plichta, M.A. Hendrickson, K.M. Abraham, A Study of the Influence of Lithium Salt Anions on Oxygen Reduction Reactions in Li-Air Batteries, J. Electrochem. Soc. 162 (2015) A1055–A1066. doi:10.1149/2.0841506jes.

[20] C.O. Laoire, S. Mukerjee, E.J. Plichta, M.A. Hendrickson, K.M. Abraham, Rechargeable Lithium/TEGDME-$LiPF_6$/O_2 Battery, J. Electrochem. Soc. 158 (2011) A302. doi:10.1149/1.3531981.

[21] C.O. Laoire, S. Mukerjee, K.M. Abraham, E.J. Plichta, M.A. Hendrickson, Influence of Nonaqueous

Solvents on the Electrochemistry of Oxygen in the Rechargeable Lithium-Air Battery, J. Phys. Chem. C. 114 (2010) 9178–9186. doi:10.1021/jp102019y.

[22] M. Maja, C. Orecchia, M. Strano, P. Tosco, M. Vanni, Effect of structure of the electrical performance of gas diffusion electrodes for metal air batteries, Electrochim. Acta. 46 (2000) 423–432. doi:10.1016/S0013-4686(00)00601-0.

[23] B. Prélot, C. Poinsignon, F. Thomas, E. Schouller, F. Villiéras, Structural-chemical disorder of manganese dioxides 1. Influence on surface properties at the solid-electrolyte interface, J. Colloid Interface Sci. 257 (2003) 77–84. doi:10.1016/S0021-9797(02)00013-9.

[24] W.X. Geping, Y.J. Zhang, Rotating Electrode Methods and Oxygen Reduction Electrocatalysts, Elsevier Science Ltd, 2015.

[25] H. Welfare, J.E. Post, Manganese oxide minerals: Crystal structures and economic and environmental significance, Proc. Natl. Acad. Sci. 96 (1999) 3447–3454. doi:10.1073/pnas.96.7.3447.

[26] K. Chen, Y. Dong Noh, K. Li, S. Komarneni, D. Xue, Microwave-Hydrothermal Crystallization of Polymorphic MnO_2 for Electrochemical Energy Storage, J. Phys. Chem. C. 117 (2013) 10770–10779. doi:10.1021/jp4018025.

[27] X. Huang, D. Lv, H. Yue, A. Attia, Y. Yang, Controllable synthesis of α- and β-MnO_2: cationic effect on hydrothermal crystallization, Nanotechnology. 19 (2008) 225606. doi:10.1088/0957-4484/19/22/225606.

[28] C. Wang, J. Ma, F. Liu, H. He, R. Zhang, The Effects of Mn^{2+} Precursors on the Structure and Ozone Decomposition Activity of Cryptomelane-Type Manganese Oxide (OMS-2) Catalysts, J. Phys. Chem. C. 119 (2015) 23119–23126. doi:10.1021/acs.jpcc.5b08095.

[29] L. Benhaddad, L. Makhloufi, B. Messaoudi, K. Rahmouni, H. Takenouti, Reactivity of Nanostructured MnO_2 in Alkaline Medium Studied with a Microcavity Electrode: Effect of Oxidizing Agent, J. Mater. Sci. Technol. 27 (2011) 585–593.

[30] L. Benhaddad, L. Makhloufi, B. Messaoudi, K. Rahmouni, H. Takenouti, Reactivity of Nanostructured MnO_2 in Alkaline Medium Studied with a Micro-Cavity Electrode: Effect of Synthesizing Temperature, ACS Appl. Mater. Interfaces. 1 (2009) 424–432. doi:10.1021/am800118y.

[31] T. Maoka, Electrochemical reduction of oxygen on small platinum particles supported on carbon in

concentrated phosphoric acid - Effects of platinum content in the catalyst layer and operating temperature of the electrode, Electrochim. Acta. 33 (1988) 371–377.

[32] M.L. Calegaro, F.H.B. Lima, E.A. Ticianelli, Oxygen reduction reaction on nanosized manganese oxide particles dispersed on carbon in alkaline solutions, J. Power Sources. 158 (2006) 735–739. doi:10.1016/j.jpowsour.2005.08.048.

[33] J.J. Salvador-Pascual, A. Chávez-Carvayar, O. Solorza-Feria, Synthesis and characterization of PdSn oxygen reduction electrocatalyst, ECS Trans. 15 (2008) 3.

[34] Y. Ma, H. Wang, S. Ji, J. Goh, H. Feng, R. Wang, Highly active Vulcan carbon composite for oxygen reduction reaction in alkaline medium, Electrochim. Acta. 133 (2014) 391–398. doi:10.1016/j.electacta.2014.04.080.

[35] J. Jiang, K. Rajagopalan, Oxygen reduction reaction on a mini gas diffusion electrode, Electrochim. Acta. 58 (2011) 717–722. doi:10.1016/j.electacta.2011.10.022.

[36] J. Seo, D.H. Anjum, K. Takanabe, J. Kubota, K. Domen, Electrodeposited Ultrafine TaO_x/CB Catalysts for PEFC Cathode Application: Their Oxygen Reduction Reaction Kinetics, Electrochim. Acta. 149 (2014) 76–85. doi:10.1016/j.electacta.2014.10.073.

[37] M. Li, T. Liu, L. Fan, X. Bo, L. Guo, Three-dimensional hierarchical meso/macroporous Fe/Co-nitrogen-doped carbon encapsulated FeCo alloy nanoparticles prepared without any template or surfactant: High-performance bifunctional oxygen electrodes, J. Alloys Compd. 686 (2016) 467–478. doi:10.1016/j.jallcom.2016.06.060.

[38] V. Jovancicevic, O.M. Bockris, The Mechanism of Oxygen Reduction on Iron in Neutral Solutions, J. Electrochem. Soc. 133 (1986) 1797. doi:10.1149/1.2109021.

[39] K. Suárez-Alcántara, A. Rodríguez-Castellanos, R. Dante, O. Solorza-Feria, $Ru_xCr_ySe_z$ electrocatalyst for oxygen reduction in a polymer electrolyte membrane fuel cell, J. Power Sources. 157 (2006) 114–120. doi:10.1016/j.jpowsour.2005.07.065.

[40] S. Ardizzone, C.L. Bianchi, D. Tirelli, Mn_3O_4 and γ-MnOOH powders, preparation, phase composition and XPS characterisation, Colloids Surfaces A Physicochem. Eng. Asp. 134 (1998) 305–312.

[41] D. Costa, P. Marcus, W.P. Yang, Resistance to Pitting and Chemical Composition of Passive Films of

a Fe-17%Cr Alloy in Chloride-Containing Acid Solution, J. Electrochem. Soc. 141 (1994) 2669–2676.

Table 1. Oxygen Reduction Reaction (ORR) shift by *S*-LSVs and kinetic parameters by Tafel elaboration (-*b*), both in aqueous and organic media. The analyses have been performed at constant temperature, T = 298 ± 1 K.

Solvent/electrolyte	Cathode	ORR shift (mV)	-*b* (mV dec^{-1})
Water/0.1 M KOH	**no MnO_2**	–	53
	MS_N	100	100
	MS_K	100	87
	MCl_K	95	160
TEGDME/0.5 M $LiNO_3$	**no MnO_2**	–	40
	MS_N	80	27
	MS_K	107	30
	MCl_K	95	28

Table 2. XPS data as Binding Energies (B. E., according to the references [40,41]) and the counts ratio for the different O 1s species, for all the synthesized nanopowders.

O 1s	MS_N		MS_K		MCl_K	
	B. E. (eV)	**Ratio**	**B. E. (eV)**	**Ratio**	**B. E. (eV)**	**Ratio**
O^{2-} lattice	529.5	0.64	529.7	0.71	529.7	0.68
-OH	531.0	0.23	531.2	0.19	531.2	0.23
H_2O chemisorbed	532.2	0.13	532.5	0.10	532.4	0.09

Figure captions

Figure 1. XRPD spectra for all the synthesized nanopowders (100% intensity reflection planes have been highlighted for the detected polymorphs).

Figure 2. TEM images of **a)** MS_N, **b)** MS_K and **c)** MCl_K samples.

Figure 3. Pore size distribution from BET analysis for all the synthesized samples. Surface area values (S_{BET}) have been reported near the histograms.

Figure 4. ORR Staircase-Linear Sweep Voltammetries relative to all the prepared cathodes in **a)** water/0.1 M KOH and **b)** TEGDME/0.5 M $LiNO_3$ (the onset potentials have been highlighted). *S*-LSV were performed by applying for 10 s a step potential of 10 mV (scan rate of 1 mV s^{-1}, the current was recorded at the end of each potential step).

Figure 5. Tafel plots for the ORR both in water/0.1 M KOH and TEGDME/0.5 $LiNO_3$, determined by *S*-LSV scans (values of -*b* slopes have been reported).

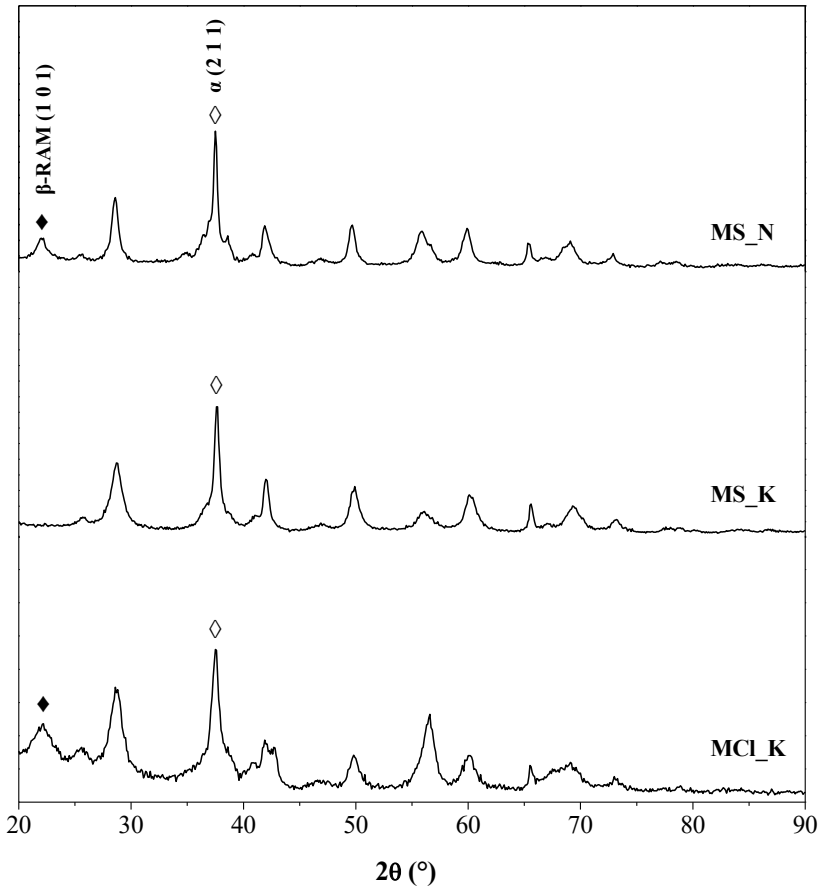

FIGURE 1

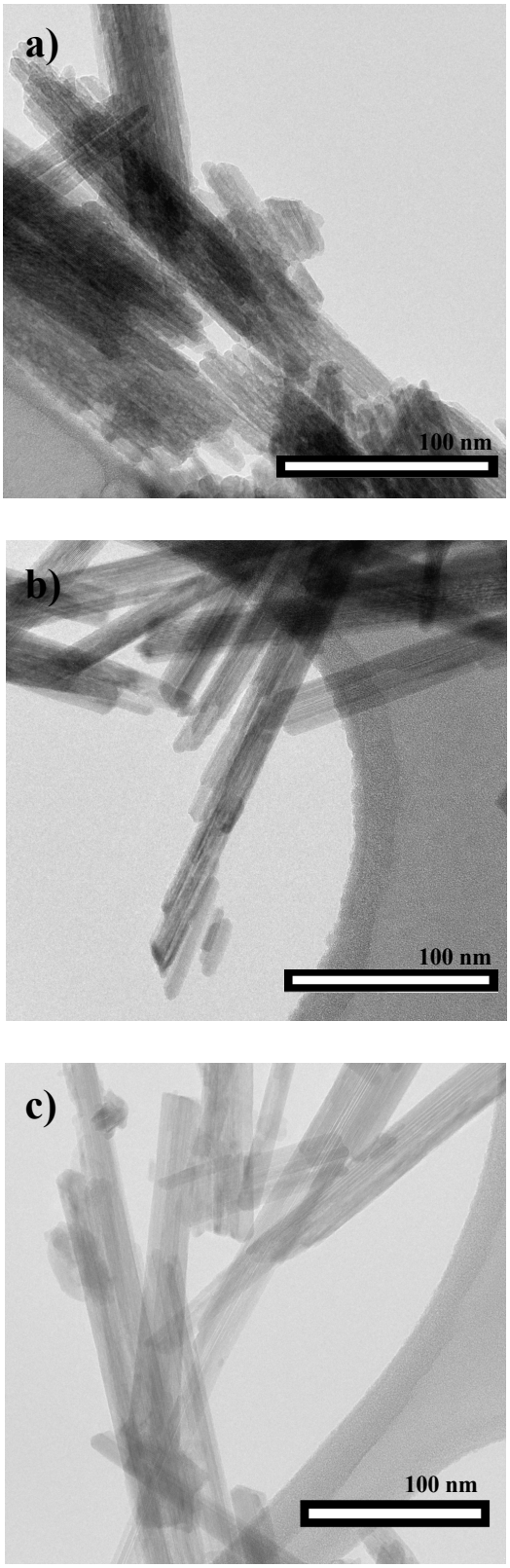

FIGURE 2

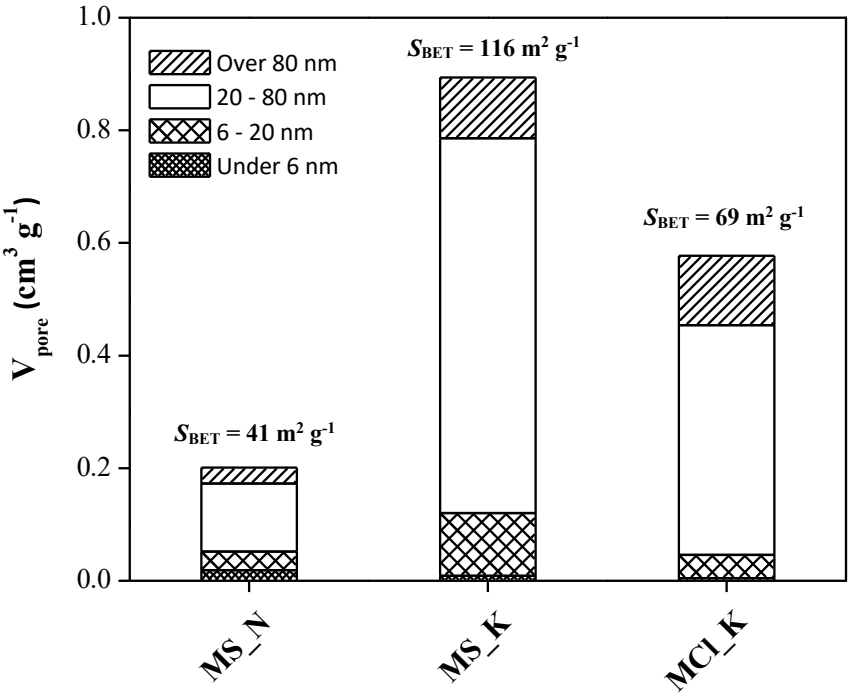
1.0
0.8
0.6
0.4
0.2
0.0
V_{pore} (cm^3 g^{-1})
Over 80 nm
20 - 80 nm
6 - 20 nm
Under 6 nm
S_{BET} = 41 m^2 g^{-1}
S_{BET} = 116 m^2 g^{-1}
S_{BET} = 69 m^2 g^{-1}
MS_N
MS_K
MCl_K

FIGURE 3

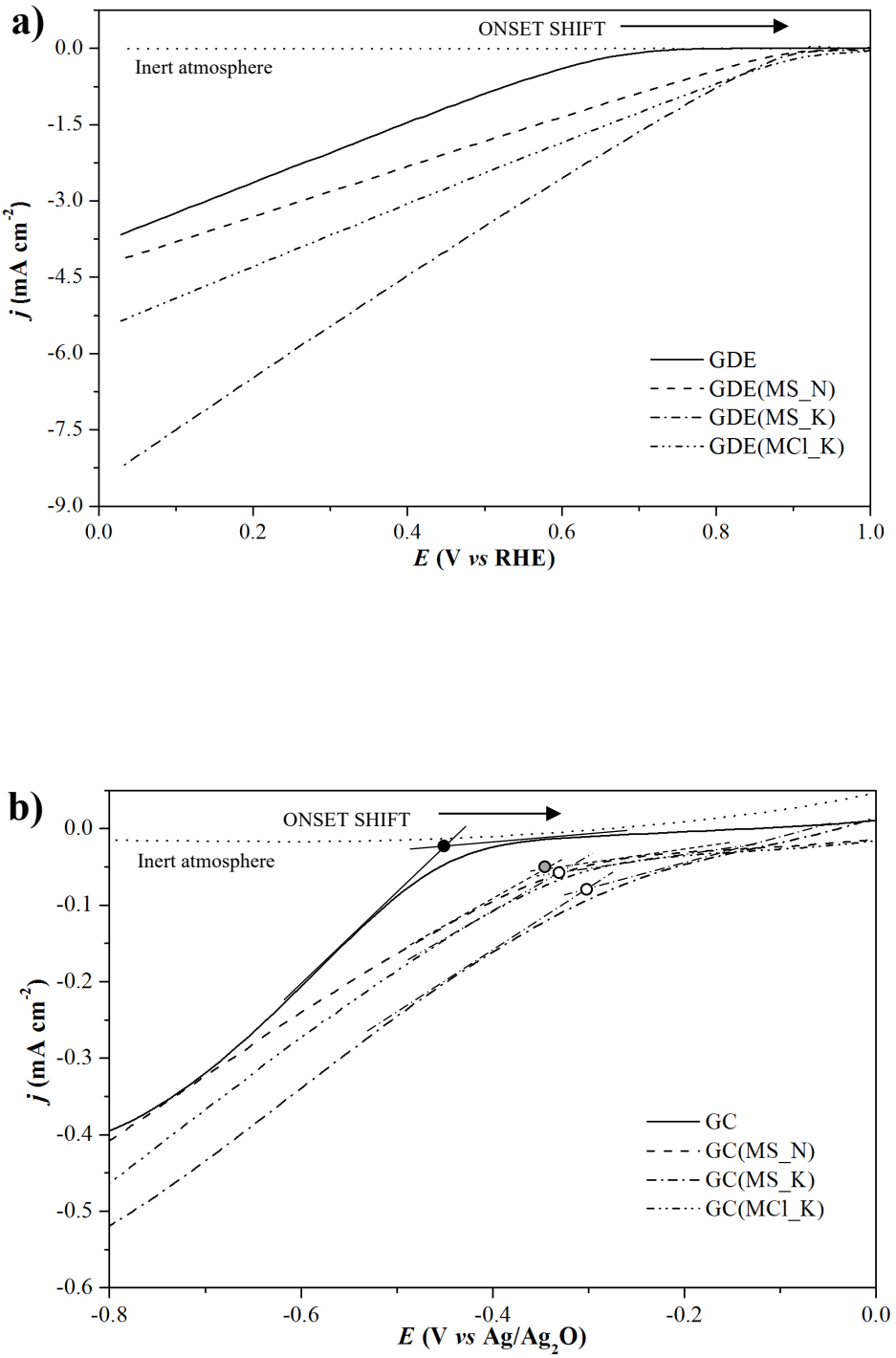
a)
ONSET SHIFT
Inert atmosphere
0.0
-1.5
-3.0
-4.5
-6.0
-7.5
-9.0
j (mA cm-2)
0.0
0.2
0.4
0.6
0.8
1.0
E (V vs RHE)
GDE
GDE(MS_N)
GDE(MS_K)
GDE(MCl_K)
b)
ONSET SHIFT
Inert atmosphere
0.0
-0.1
-0.2
-0.3
-0.4
-0.5
-0.6
j (mA cm-2)
-0.8
-0.6
-0.4
-0.2
0.0
E (V vs Ag/Ag2O)
GC
GC(MS_N)
GC(MS_K)
GC(MCl_K)

FIGURE 4

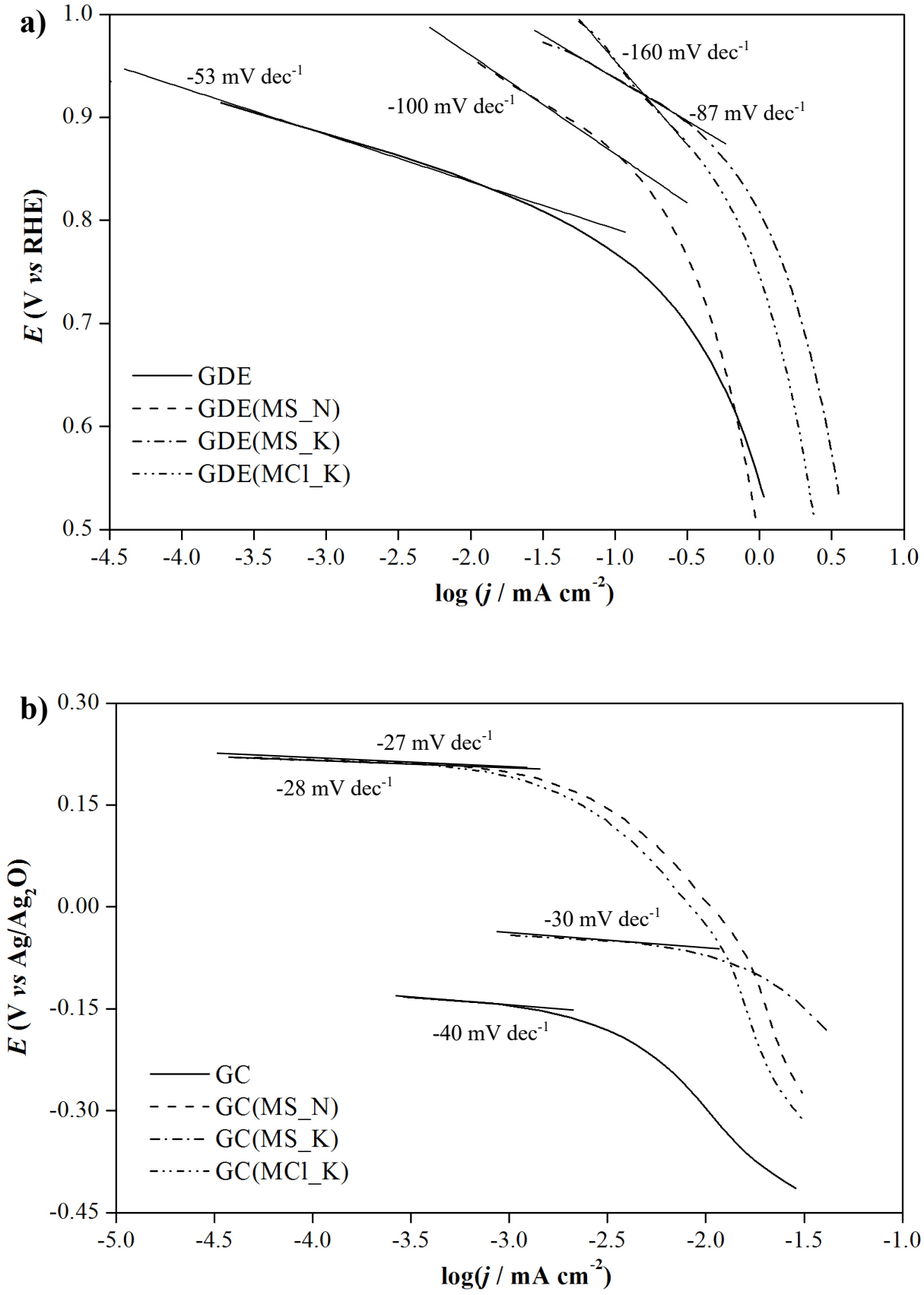
a)
-53 mV dec-1
-100 mV dec-1
-160 mV dec-1
-87 mV dec-1
GDE
GDE(MS_N)
GDE(MS_K)
GDE(MCl_K)
E (V vs RHE)
log (j / mA cm-2)
b)
-27 mV dec-1
-28 mV dec-1
-30 mV dec-1
-40 mV dec-1
GC
GC(MS_N)
GC(MS_K)
GC(MCl_K)
E (V vs Ag/Ag2O)
log(j / mA cm-2)

FIGURE 5